Research Square

Preprints are preliminary reports that have not undergone peer review.
They should not be considered conclusive, used to inform clinical practice,
or referenced by the media as validated information.

Experimental and numerical investigation of frequency-selective localisation of flexural waves in a locally resonant rainbow meta-lattice

Subhasish Sarkar

subhasishs@iisc.ac.in

Indian Institute of Science Bangalore https://orcid.org/0009-0008-5897-3418

Avinash Umashankar

Indian Institute of Science Bangalore https://orcid.org/0009-0006-3194-8306

Srinivasan Gopalakrishnan

Indian Institute of Science Bangalore https://orcid.org/0000-0001-6165-6132

Research Article

Keywords: Locally resonant metamaterials, Bandgaps, Flexural vibration, Rainbow trapping, Localisation, Spectral finite element method

Posted Date: November 24th, 2026

DOI: https://doi.org/10.21203/rs.3.rs-11860382/v1

License: This work is licensed under a Creative Commons Attribution 4.0 International License.
Read Full License

Additional Declarations: The authors declare no competing interests.

Experimental and numerical investigation of frequency-selective localisation of flexural waves in a locally resonant rainbow meta-lattice

Subhasish Sarkar[a,*], Avinash Umashankar[a], Srinivasan Gopalakrishnan[a]

[a]*Department of Aerospace Engineering, Indian Institute of Science, CV Raman Road, Bengaluru, 560012, Karnataka, India*

Abstract

Frequency-selective localisation of out-of-plane flexural waves is investigated numerically and experimentally in a graded planar meta-lattice comprising X-shaped tetracantilever locally resonant (X-TCLR) unit cells. Each unit cell incorporates four inclined cantilever resonators integral with a continuous primary beam, allowing geometric tuning through the resonator-arm length while maintaining uniform primary-beam geometry, member cross-sections and cell spacing. The spectral finite element method (SFEM), incorporating Timoshenko flexure and Saint–Venant torsion, is employed to investigate the Bloch dispersion characteristics and steady-state harmonic responses. The unit-cell dispersion reveals a locally resonant bandgap (LRBG) containing a nearly flat branch whose frequency closely matches the first bending natural frequency of the corresponding isolated cantilever, with deformation concentrated in the resonator arms. Increasing the resonator-arm length from 21 to 24 mm shifts the lower edge of this region from 4589.67 to 3797.24 Hz,

*Corresponding author.
Email address: subhasishs@iisc.ac.in (Subhasish Sarkar)

providing a geometrically tunable range of local propagation limits. In the seven-cell graded meta-lattice, cell-wise localisation fractions and frequency–position maps reveal spatially ordered flexural responses, with successive unit cells dominating over distinct frequency intervals. Experiments on a fabricated meta-lattice reproduce the predicted ordering at selected frequencies and across the localisation map, enabling quantitative comparison of the corresponding frequency intervals. The results establish a relationship between resonator geometry, local dispersion characteristics and frequency-dependent spatial localisation of flexural vibrations in a finite structural lattice.
Keywords: Locally resonant metamaterials, Bandgaps, Flexural vibration, Rainbow trapping, Localisation, Spectral finite element method

1. Introduction

Planar structural lattices comprising interconnected slender members offer opportunities to tailor out-of-plane vibration through geometric design. Their dynamic behaviour is governed by the flexural and torsional deformation of the constituent members, together with the interaction between the continuous supporting structure and local resonant elements. Controlling these interactions provides a means of modifying the spatial distribution of vibrational responses over selected frequency ranges. Within this context, phononic crystals and elastic metamaterials offer versatile platforms for controlling elastic-wave propagation through engineered periodicity and local resonance. Tailoring their structural features enables bandgap formation [1, 2, 3] and wave phenomena such as negative refraction [4], wave focusing [5] and topologically protected transport [6]. These capabilities support appli-

cations in vibration isolation [7, 8], vibration attenuation [9, 10, 11], energy harvesting [12, 13, 14], impact mitigation [15] and nondestructive evaluation [16]. Spatial variation of the unit-cell geometry further provides a route to controlling the frequency-dependent distribution of flexural responses within finite structural lattices.

Bandgaps in phononic crystals and elastic metamaterials commonly arise through Bragg scattering or local resonance mechanisms. Bragg bandgaps originate from interference associated with periodic scattering, providing a means of frequency-selective wave filtering through structural periodicity [17]. More broadly, geometric control of lattice dispersion and directional propagation has been explored through carbon-fibre-reinforced polymer lattices [18], chiral and auxetic honeycombs [19, 2], auxiliary semicircular rings [20], tooth-shaped attachments [21] and topology optimisation [22]. Geometrically tunable low-frequency bandgaps have also been reported in chiral metamaterial structures [23], highlighting the sensitivity of lattice dynamics to structural design. Nevertheless, conventional Bragg bandgaps occur at wavelengths comparable to the lattice periodicity, so extending this mechanism to low frequencies generally requires larger unit cells [24].

Locally resonant metamaterials address this scale limitation through the coupling of resonator dynamics with the host structure, enabling attenuation at wavelengths substantially larger than the unit-cell dimensions. Local resonance (LR) mechanisms have been employed to suppress flexural and torsional waves [25, 26] and incorporated into square beam grids [27], functionally graded square and hexagonal lattices [28], and architectures containing auxiliary resonators or variable-cross-section members [7, 29]. Continuous

structural resonators include cantilever members supporting multiple flexural resonances [30], bending–torsion-coupled members for multimodal attenuation [31] and spider-web-inspired beam networks [32, 33]. However, their attenuation bandwidth and modal coverage depend on resonator tuning and host–resonator coupling, motivating strategies involving combined Bragg and LR effects [24], nonlinear oscillators [34], electromagnetic resonators with multiple coupled frequencies [35] and additional damping [36]. The tunability of LR dynamics also provides a basis for graded architectures that spatially control elastic-wave propagation.

Rainbow trapping provides a means of spatially separating and localising different frequency components within a graded structure, analogous to the separation of colours in an optical rainbow. This behaviour arises from spatial variations in local dispersion characteristics, which cause different frequencies to encounter regions of reduced group velocity at distinct positions, promoting wave slowing and enhanced localised responses [37]. Experimental demonstrations include ultrasonic guided waves in chirped phononic crystal plates [38], frequency-dependent penetration and reflection of torsional waves in chirped metallic beams [39], and radial localisation in axisymmetric grooved plates [40]. In beam grid lattices, grading the unit-cell aspect ratio enabled out-of-plane wave concentration [41], while nonperiodic mass blocks connected by curved beams broadened attenuation bands in two-dimensional rainbow metamaterials [42]. Related geometric implementations include guided-wave turning in variable-cross-section switch rails [43] and flexural-wave trapping and vibration suppression in annular acoustic black hole metasurfaces combining thickness tapering with radial

periodicity [44]. The combination of rainbow trapping and structural resonance has further been investigated for piezoelectric energy harvesting in periodically perforated beams [45] and thickness-modulated Euler–Bernoulli beams [46]. Frequency-dependent localisation has also been investigated through bandgap and interface-state effects in sinusoidal-profile nonuniform beams [47]. Extensions to topological metamaterials include rainbow trapping, concentration and guiding in graded elastic valley phononic crystal plates [48], and rainbow trapping with piezoelectric energy harvesting in acoustic phononic crystals with graded coupled interfaces [49]. Zheng et al. [50] demonstrated an on-chip elastic rainbow formed by spatially separated bulk Landau-level modes and its capture by topological chiral edge states. Chen et al. [51] further investigated reconfigurable topological gradient metamaterials, demonstrating elastic-wave rainbow trapping and localised responses through spatial variations in structural parameters.

Rainbow metamaterials with graded local resonators provide a complementary route by varying resonance frequencies and associated propagation limits while retaining a uniform host geometry. Zhao et al. [52] numerically demonstrated broadband Lamb-wave trapping by varying the cap masses of textured stub resonators in cellular metamaterial plates. De Ponti et al. [53] combined resonator-length grading with broken geometrical symmetry to obtain flexural-wave localisation and conversion into reflected torsional waves. Experiments on graded cantilever arrays also established enhanced energy harvesting, with measured space–frequency responses compared with local dispersion predictions [54]. Numerical investigations of hybrid mechanical and electromechanical metastructures have demonstrated enhanced har-

vesting and wider attenuation ranges, while examining the contributions of grading-induced localised modes and individual resonators to the power output [55].

For unit cells incorporating beam-type local resonators, Liu et al. [56] demonstrated configurations in which the natural frequencies of cantilever-type resonators lie within locally resonant attenuation regions. Serrano et al. [57] subsequently showed that this correspondence depends on the coupled dynamics of the resonators and the supporting structure. These findings emphasise the relationship between individual resonator dynamics and the dispersion characteristics of the assembled lattice. Although graded resonant structures have previously demonstrated frequency-dependent wave localisation, relating the geometric variation of local propagation limits to the frequency intervals of dominant vibration in a finite structure remains an important design consideration.

In this study, a rainbow meta-lattice made up of X-shaped tetracantilever locally resonant (X-TCLR) unit cells is investigated for frequency-selective localisation of out-of-plane flexural waves. Each unit cell comprises four inclined cantilever resonators integral with a continuous primary beam, forming a planar resonant structural network. The inclined resonator-arm length L_r serves as the geometric tuning parameter, allowing the local dynamic characteristics to be modified without changing the primary-beam geometry, member cross-sections or unit-cell spacing. The Bloch dispersion characteristics are investigated using the spectral finite element method (SFEM), incorporating Timoshenko flexure and Saint–Venant torsion. For the considered configuration, a nearly flat dispersion branch within the locally resonant

bandgap (LRBG) region closely corresponds to the first bending natural frequency of the isolated cantilever, with the associated deformation concentrated in the resonator arms. The variation of the lower bandgap edge with L_r is then used to identify the frequency range relevant to spatial localisation.

A finite graded meta-lattice is subsequently investigated under steady-state harmonic excitation. The spatial distribution of flexural responses is quantified through cell-wise localisation fractions and frequency–position localisation maps, which identify successive dominant unit cells over distinct frequency intervals. Experiments on a fabricated seven-cell X-TCLR meta-lattice validate the predicted ordering of the dominant response locations and provide a quantitative comparison of the corresponding frequency intervals. By relating the geometric variation of the local resonators to the evolution of the local propagation limits and the resulting finite-structure response, this study characterises a geometrically controlled mechanism of spatial frequency selection. The numerical and experimental results provide a basis for developing structural lattices exhibiting frequency-selective flexural vibration localisation, with potential applications in sensing and vibration energy harvesting.

2. Unit cell geometry

The X-TCLR unit cell and the finite meta-lattice are shown in Fig. 1. The unit cell has a periodic length of a and repeats along one principal direction to form the finite meta-lattice. The primary horizontal member provides continuity between adjacent unit cells, while the four inclined cantilever-type beams are connected rigidly to the central junction and act as local

resonators. The length of each cantilever-type local resonator, measured from the central junction to its free end, is denoted by L_r, with each resonator oriented at an angle of 60° with respect to the primary horizontal member. The X-TCLR configuration therefore forms an integral planar network of beam-like members, in which the primary beam provides structural continuity between adjacent cells and the inclined cantilevers act as local resonant elements. This arrangement enables modification of the local flexural dynamics through the resonator geometry without altering the continuous primary-beam path.

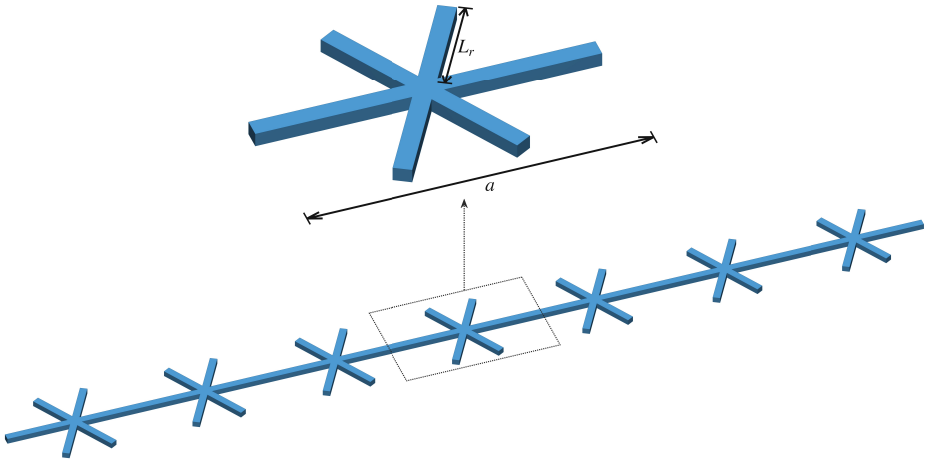


Figure 1: Schematic of the finite meta-lattice and the corresponding X-TCLR unit cell.

All members are modelled as prismatic beams with identical rectangular cross-sections and isotropic material properties. The geometric and material properties adopted in the numerical analysis are summarised in Table 1.

Table 1: Geometric and material properties of the locally resonant meta-lattice.

Property	Lattice constant, a	Cross-sectional width, b	Cross-sectional thickness, d	Young's modulus, E	Poisson's ratio, ν	Mass density, ρ
Value	0.07 m	0.00375 m	0.003 m	200 GPa	0.3	7850 kg m^{-3}

3. Methodology

3.1. Dynamic stiffness formulation

The planar meta-lattice consists of periodically arranged X-TCLR unit cells composed of grid members rigidly connected at their joints. Each grid member is modelled by combining a Timoshenko beam formulation for out-of-plane flexural motion, including shear deformation and rotary inertia, with a Saint–Venant shaft formulation for torsional motion. Consider a straight, uniform grid member of length L contained in the global X–Y plane. The local x-axis is directed from node 1 to node 2, the local y-axis lies in the grid plane, and the local z-axis is normal to that plane. The member is inclined at an angle α to the global X-axis, as shown in Fig. 2. The out-of-plane motion is described by the transverse displacement $w(x,t)$, torsional rotation $\phi(x,t)$, and bending rotation $\psi(x,t)$. The member is assumed to be straight, prismatic, centroidal, linearly elastic, and subjected to small-amplitude motion. Under these assumptions, the out-of-plane variables (w,ϕ,ψ) are independent of the in-plane variables (u,v,θ) at the member level [17].

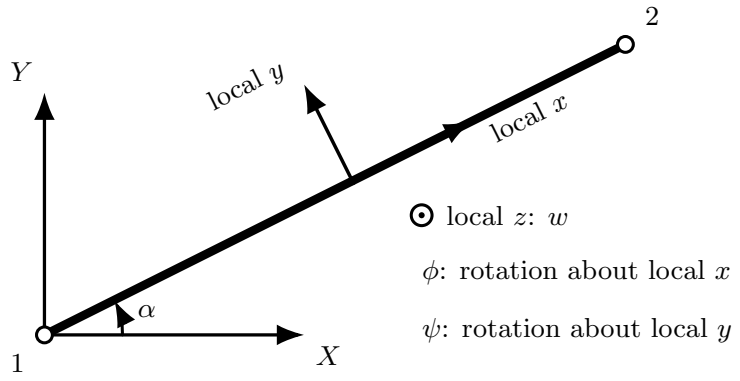


Figure 2: Local coordinates and out-of-plane kinematics of an inclined grid member.

For time-harmonic motion, the field variables are expressed as

$$\begin{aligned} w(x,t) &= W(x)\exp(\mathrm{i}\omega t), \\ \psi(x,t) &= \Psi(x)\exp(\mathrm{i}\omega t), \\ \phi(x,t) &= \Phi(x)\exp(\mathrm{i}\omega t). \end{aligned} \tag{1}$$

where ω is the circular frequency and $\mathrm{i} = \sqrt{-1}$.

3.1.1. Spectral Timoshenko beam formulation

The flexural motion is represented using Timoshenko beam theory, including shear deformation and rotary inertia. The governing equations are given by

$$\kappa GA\frac{\partial}{\partial x}\left(\frac{\partial w}{\partial x} - \psi\right) = \rho A\frac{\partial^2 w}{\partial t^2}, \tag{2}$$

$$EI_y\frac{\partial^2 \psi}{\partial x^2} + \kappa GA\left(\frac{\partial w}{\partial x} - \psi\right) = \rho I_y\frac{\partial^2 \psi}{\partial t^2}. \tag{3}$$

Here, E and G are Young's modulus and shear modulus, respectively, ρ is the material density, A is the cross-sectional area, I_y is the second moment

of area about the local y-axis, and κ is the shear correction factor. The shear force and bending moment are

$$\begin{aligned} Q_z(x,t) &= \kappa GA\left(\frac{\partial w}{\partial x} - \psi\right), \\ M_y(x,t) &= EI_y\frac{\partial \psi}{\partial x}. \end{aligned} \tag{4}$$

For an individual travelling-wave component,

$$\begin{aligned} w(x,t) &= W_0\exp(-\mathrm{i}(kx-\omega t)), \\ \psi(x,t) &= \Psi_0\exp(-\mathrm{i}(kx-\omega t)). \end{aligned} \tag{5}$$

Substitution into Eqs. (2) and (3) gives

$$\begin{bmatrix} \rho A\omega^2 - \kappa GAk^2 & \mathrm{i}\kappa GAk \\ -\mathrm{i}\kappa GAk & \rho I_y\omega^2 - EI_yk^2 - \kappa GA \end{bmatrix}\begin{bmatrix} W_0 \\ \Psi_0 \end{bmatrix} = \begin{bmatrix} 0 \\ 0 \end{bmatrix}. \tag{6}$$

The condition for a non-trivial solution yields

$$\begin{aligned} \kappa GA\,EI_yk^4 - \omega^2\left(\rho AEI_y + \kappa GA\rho I_y\right)k^2 \\ + \rho A\rho I_y\omega^4 - \rho A\kappa GA\omega^2 = 0. \end{aligned} \tag{7}$$

The two roots in k^2, denoted by $\lambda_\pm$, are

$$\begin{aligned} \lambda_\pm = \frac{1}{2\kappa GA\,EI_y}\Bigg[&\omega^2\left(\rho AEI_y + \kappa GA\rho I_y\right) \\ &\pm\Bigg\{\omega^4\left(\rho AEI_y + \kappa GA\rho I_y\right)^2 \\ &\quad - 4\kappa GA\,EI_y\left(\rho A\rho I_y\omega^4 - \rho A\kappa GA\omega^2\right)\Bigg\}^{1/2}\Bigg]. \end{aligned} \tag{8}$$

The corresponding four flexural wavenumbers are

$$k_1 = \sqrt{\lambda_+},\quad k_2 = -\sqrt{\lambda_+},\quad k_3 = \sqrt{\lambda_-},\quad k_4 = -\sqrt{\lambda_-} \tag{9}$$

For each root, the rotation and transverse-displacement amplitudes satisfy

$$\begin{aligned} \Psi_j &= \beta_j W_j, \\ \beta_j &= \mathrm{i}\frac{\rho A\omega^2 - \kappa G A k_j^2}{\kappa G A k_j}, \\ &= -\mathrm{i}\left(k_j - \frac{\rho A\omega^2}{\kappa G A k_j}\right). \end{aligned} \tag{10}$$

The exact spectral fields are therefore

$$\begin{aligned} W(x) &= \sum_{j=1}^{4} C_j \exp(-\mathrm{i}k_j x), \\ \Psi(x) &= \sum_{j=1}^{4} \beta_j C_j \exp(-\mathrm{i}k_j x). \end{aligned} \tag{11}$$

With $\eta_j = \exp(-\mathrm{i}k_j L)$, define the nodal flexural displacement vector and spectral coefficient vector as

$$\begin{aligned} \boldsymbol{d}_\mathrm{b} &= \begin{bmatrix} W(0) & \Psi(0) & W(L) & \Psi(L) \end{bmatrix}^\mathrm{T}, \\ \boldsymbol{c} &= \begin{bmatrix} C_1 & C_2 & C_3 & C_4 \end{bmatrix}^\mathrm{T}. \end{aligned} \tag{12}$$

Evaluation of the spectral fields at the member ends gives

$$\begin{aligned} \boldsymbol{d}_\mathrm{b} &= \boldsymbol{T}_1(\omega)\boldsymbol{c}, \\ \boldsymbol{T}_1(\omega) &= \begin{bmatrix} 1 & 1 & 1 & 1 \\ \beta_1 & \beta_2 & \beta_3 & \beta_4 \\ \eta_1 & \eta_2 & \eta_3 & \eta_4 \\ \beta_1\eta_1 & \beta_2\eta_2 & \beta_3\eta_3 & \beta_4\eta_4 \end{bmatrix}. \end{aligned} \tag{13}$$

After suppressing the common harmonic time factor, the frequency-domain

force resultants are

$$\begin{aligned} Q_z(x) &= \kappa GA\left(\frac{dW}{dx} - \Psi\right), \\ M_y(x) &= EI_y\frac{d\Psi}{dx}. \end{aligned} \tag{14}$$

Using outward-positive member-end forces,

$$\begin{aligned} \boldsymbol{f}_{\mathrm{b}} &= \begin{bmatrix} -Q_z(0) & -M_y(0) & Q_z(L) & M_y(L) \end{bmatrix}^{\mathrm{T}}, \\ &= \boldsymbol{T}_2(\omega)\boldsymbol{c}. \end{aligned} \tag{15}$$

where

$$\boldsymbol{T}_2(\omega) = \begin{bmatrix} \kappa GA(\mathrm{i}k_1+\beta_1) & \kappa GA(\mathrm{i}k_2+\beta_2) & \kappa GA(\mathrm{i}k_3+\beta_3) & \kappa GA(\mathrm{i}k_4+\beta_4) \\ \mathrm{i}EI_y k_1\beta_1 & \mathrm{i}EI_y k_2\beta_2 & \mathrm{i}EI_y k_3\beta_3 & \mathrm{i}EI_y k_4\beta_4 \\ -\kappa GA(\mathrm{i}k_1+\beta_1)\eta_1 & -\kappa GA(\mathrm{i}k_2+\beta_2)\eta_2 & -\kappa GA(\mathrm{i}k_3+\beta_3)\eta_3 & -\kappa GA(\mathrm{i}k_4+\beta_4)\eta_4 \\ -\mathrm{i}EI_y k_1\beta_1\eta_1 & -\mathrm{i}EI_y k_2\beta_2\eta_2 & -\mathrm{i}EI_y k_3\beta_3\eta_3 & -\mathrm{i}EI_y k_4\beta_4\eta_4 \end{bmatrix}. \tag{16}$$

Eliminating $\boldsymbol{c}$ yields the exact Timoshenko dynamic stiffness relation

$$\begin{aligned} \boldsymbol{f}_{\mathrm{b}} &= \boldsymbol{K}_{\mathrm{b}}(\omega)\boldsymbol{d}_{\mathrm{b}}, \\ \boldsymbol{K}_{\mathrm{b}}(\omega) &= \boldsymbol{T}_2(\omega)\boldsymbol{T}_1^{-1}(\omega). \end{aligned} \tag{17}$$

The same matrix may alternatively be expressed in the symmetric closed form

$$\boldsymbol{K}_{\mathrm{b}}(\omega) = \begin{bmatrix} d_1 & d_2 & d_4 & d_5 \\ d_2 & d_3 & -d_5 & d_6 \\ d_4 & -d_5 & d_1 & -d_2 \\ d_5 & d_6 & -d_2 & d_3 \end{bmatrix}. \tag{18}$$

To define the frequency-dependent coefficients, introduce the dimensionless parameters

$$\bar{b}^2 = \frac{\rho A\omega^2 L^4}{EI_y}, \quad r^2 = \frac{I_y}{AL^2}, \quad \sigma^2 = \frac{EI_y}{\kappa GAL^2}, \quad \Delta = r^2+\sigma^2 \tag{19}$$

Here, $\bar{b}$ denotes the positive square root of the first expression in Eq. (19). Define

$$\mathcal{R} = \sqrt{\frac{\Delta^2}{4} + \frac{1 - \bar{b}^2 r^2 \sigma^2}{\bar{b}^2}}. \tag{20}$$

For $\bar{b}^2 r^2 \sigma^2 < 1$, λ_1 and λ_2 are real and generate oscillatory and hyperbolic terms, respectively. For $\bar{b}^2 r^2 \sigma^2 > 1$, λ_2 is purely imaginary, and the same expressions are interpreted using complex arithmetic. The dimensionless roots are defined as

$$\lambda_1 = \bar{b}\sqrt{\frac{\Delta}{2} + \mathcal{R}}, \quad \lambda_2 = \bar{b}\sqrt{-\frac{\Delta}{2} + \mathcal{R}} \tag{21}$$

For compactness, let

$$s_1 = \sin\lambda_1, \quad c_1 = \cos\lambda_1, \quad S_2 = \sinh\lambda_2, \quad C_2 = \cosh\lambda_2. \tag{22}$$

The auxiliary amplitude quantities are

$$\chi_1 = \frac{\lambda_1^2 - \bar{b}^2\sigma^2}{\lambda_1}, \quad \chi_2 = \frac{\lambda_2^2 + \bar{b}^2\sigma^2}{\lambda_2} \tag{23}$$

The positive sign in the expression for χ_2 follows from the hyperbolic root. The remaining quantities are

$$\begin{aligned} \eta &= \frac{\chi_1}{\chi_2}, \\ \delta &= 2\eta(1 - c_1 C_2) + (1 - \eta^2) s_1 S_2, \\ R_j &= \frac{EI_y}{L^j}, \qquad j = 1, 2, 3. \end{aligned} \tag{24}$$

The six independent flexural coefficients are

$$
\begin{aligned}
d_1 &= \frac{R_3\bar{b}^2(\lambda_2+\eta\lambda_1)(c_1S_2+\eta s_1C_2)}{\lambda_1\lambda_2\delta},\\
d_2 &= \frac{R_2\chi_1}{\delta}\left[(\lambda_1+\eta\lambda_2)s_1S_2-(\lambda_2-\eta\lambda_1)(1-c_1C_2)\right],\\
d_3 &= \frac{R_1(\lambda_2+\eta\lambda_1)(s_1C_2-\eta c_1S_2)}{\delta},\\
d_4 &= -\frac{R_3\bar{b}^2(\lambda_2+\eta\lambda_1)(S_2+\eta s_1)}{\lambda_1\lambda_2\delta},\\
d_5 &= \frac{R_2\chi_1(\lambda_2+\eta\lambda_1)(C_2-c_1)}{\delta},\\
d_6 &= \frac{R_1(\lambda_2+\eta\lambda_1)(\eta S_2-s_1)}{\delta}
\end{aligned}
\tag{25}
$$

Equations (17) and (18) are algebraically equivalent. The former is convenient for numerical implementation, whereas Eqs. (19)–(25) explicitly provide the individual frequency-dependent matrix entries [58, 59].

3.1.2. Spectral torsional formulation

The torsional rotation $\phi(x,t)$ is governed by the Saint–Venant shaft equation

$$
GJ\frac{\partial^2\phi}{\partial x^2}=\rho I_p\frac{\partial^2\phi}{\partial t^2},
\tag{26}
$$

where J is the Saint–Venant torsion constant and I_p is the polar second moment of area associated with rotary inertia. Substitution of $\phi=\Phi_0\exp(-\mathrm{i}(k_{\mathrm{t}}x-\omega t))$ gives

$$
GJk_{\mathrm{t}}^2-\rho I_p\omega^2=0,\quad k_{\mathrm{t}}^2=\omega^2\frac{\rho I_p}{GJ}
\tag{27}
$$

where k_{t} denotes the torsional wavenumber

The exact torsional field and corresponding internal torque are

$$\begin{aligned} \Phi(x) &= D_1 \exp(-\mathrm{i}k_\mathrm{t}x) + D_2 \exp(\mathrm{i}k_\mathrm{t}x), \\ T(x) &= GJ\frac{d\Phi}{dx}. \end{aligned} \tag{28}$$

Define the torsional nodal displacement and force vectors as

$$\begin{aligned} \boldsymbol{d}_\mathrm{t} &= \begin{bmatrix} \Phi(0) & \Phi(L) \end{bmatrix}^\mathrm{T}, \\ \boldsymbol{f}_\mathrm{t} &= \begin{bmatrix} -T(0) & T(L) \end{bmatrix}^\mathrm{T}. \end{aligned} \tag{29}$$

Elimination of D_1 and D_2 gives

$$\begin{aligned} \boldsymbol{f}_\mathrm{t} &= \boldsymbol{K}_\mathrm{t}(\omega)\boldsymbol{d}_\mathrm{t}, \\ \boldsymbol{K}_\mathrm{t}(\omega) &= \frac{GJk_\mathrm{t}}{\sin(k_\mathrm{t}L)} \begin{bmatrix} \cos(k_\mathrm{t}L) & -1 \\ -1 & \cos(k_\mathrm{t}L) \end{bmatrix}. \end{aligned} \tag{30}$$

Equation (30) is the exact torsional dynamic stiffness matrix used in the grid-member formulation [17].

3.1.3. Complete grid-member matrix, coordinate transformation, and assembly

Adopting the local nodal ordering, the displacement and force vectors are written as

$$\begin{aligned} \boldsymbol{d}^\ell_\mathrm{gr} &= \begin{bmatrix} W_1 & \Phi_1 & \Psi_1 & W_2 & \Phi_2 & \Psi_2 \end{bmatrix}^\mathrm{T}, \\ \boldsymbol{f}^\ell_\mathrm{gr} &= \begin{bmatrix} Q_1 & T_1 & M_{y1} & Q_2 & T_2 & M_{y2} \end{bmatrix}^\mathrm{T}. \end{aligned} \tag{31}$$

Here, W_r, Φ_r and Ψ_r denote the complex displacement and rotation amplitudes at member end $r = 1, 2$.

Introducing the torsional coefficients

$$\begin{aligned} t_1 &= GJk_\mathrm{t}\cot(k_\mathrm{t}L), \\ t_2 &= -GJk_\mathrm{t}\csc(k_\mathrm{t}L), \end{aligned} \tag{32}$$

the local force–displacement relation becomes

$$\boldsymbol{f}^{\ell}_{\mathrm{gr}} = \boldsymbol{K}^{\ell}_{\mathrm{gr}}(\omega)\boldsymbol{d}^{\ell}_{\mathrm{gr}}. \tag{33}$$

The complete 6×6 local dynamic stiffness matrix is

$$\boldsymbol{K}^{\ell}_{\mathrm{gr}}(\omega) = \begin{bmatrix} d_1 & 0 & d_2 & d_4 & 0 & d_5 \\ 0 & t_1 & 0 & 0 & t_2 & 0 \\ d_2 & 0 & d_3 & -d_5 & 0 & d_6 \\ d_4 & 0 & -d_5 & d_1 & 0 & -d_2 \\ 0 & t_2 & 0 & 0 & t_1 & 0 \\ d_5 & 0 & d_6 & -d_2 & 0 & d_3 \end{bmatrix}. \tag{34}$$

The members have doubly symmetric cross-sections, with coincident centroids and shear centres, and local axes aligned with the principal bending axes. The zero entries indicate the absence of direct bending–torsion coupling for a straight centroidal member. Both components nevertheless contribute to the global lattice response after coordinate transformation and assembly.

Let $c = \cos\alpha$ and $s = \sin\alpha$. The global nodal displacement and force vectors are

$$\begin{aligned} \boldsymbol{d}^{g}_{\mathrm{gr}} &= \begin{bmatrix} W_1 & \Theta_{X1} & \Theta_{Y1} & W_2 & \Theta_{X2} & \Theta_{Y2} \end{bmatrix}^{\mathrm{T}}, \\ \boldsymbol{f}^{g}_{\mathrm{gr}} &= \begin{bmatrix} F_{Z1} & M_{X1} & M_{Y1} & F_{Z2} & M_{X2} & M_{Y2} \end{bmatrix}^{\mathrm{T}}. \end{aligned} \tag{35}$$

Since the local z-axis coincides with the global Z-axis, the local and global

displacement vectors are related through

$$\boldsymbol{d}_{\mathrm{gr}}^{\ell} = \boldsymbol{T}_{\mathrm{gr}} \boldsymbol{d}_{\mathrm{gr}}^{g},$$

$$\boldsymbol{T}_{\mathrm{gr}} = \begin{bmatrix} 1 & 0 & 0 & 0 & 0 & 0 \\ 0 & c & s & 0 & 0 & 0 \\ 0 & -s & c & 0 & 0 & 0 \\ 0 & 0 & 0 & 1 & 0 & 0 \\ 0 & 0 & 0 & 0 & c & s \\ 0 & 0 & 0 & 0 & -s & c \end{bmatrix}. \tag{36}$$

Invariance of virtual work gives

$$\begin{aligned} \boldsymbol{f}_{\mathrm{gr}}^{g} &= \boldsymbol{T}_{\mathrm{gr}}^{\mathrm{T}} \boldsymbol{f}_{\mathrm{gr}}^{\ell}, \\ \boldsymbol{K}_{\mathrm{gr}}^{g}(\omega) &= \boldsymbol{T}_{\mathrm{gr}}^{\mathrm{T}} \boldsymbol{K}_{\mathrm{gr}}^{\ell}(\omega) \boldsymbol{T}_{\mathrm{gr}} \end{aligned} \tag{37}$$

The transformed member matrices are assembled using nodal displacement compatibility and force equilibrium to obtain

$$\mathbf{K}(\omega)\mathbf{u} = \mathbf{f} \tag{38}$$

where $\mathbf{K}(\omega)$ is the assembled dynamic stiffness matrix of the unit cell or finite meta-lattice.

3.2. Bloch's theorem

For a uniform X-TCLR meta-lattice, identical unit cells repeat along the primary-beam direction with period a. Bloch's theorem allows the wave propagation characteristics of the infinite periodic lattice to be determined from a single unit cell. In the SFEM formulation, the X-TCLR unit cell is represented by seven nodes, as shown in Fig. 3. The Bloch periodic boundary

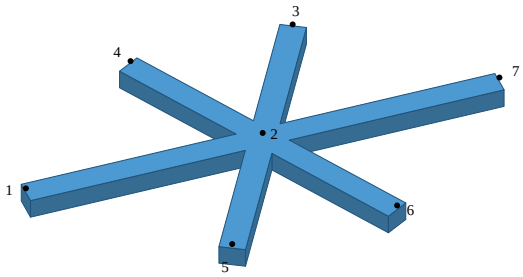


Figure 3: Node numbering of the X-TCLR unit cell used in the SFEM formulation.

conditions relating nodes 1 and 7 at the left and right unit-cell boundaries, respectively, are

$$\mathbf{u}_7 = \exp(\mathrm{i}k_x a)\mathbf{u}_1, \qquad \mathbf{f}_7 = -\exp(\mathrm{i}k_x a)\mathbf{f}_1. \tag{39}$$

Here, k_x is the Bloch wavenumber. All boundary quantities are expressed in the same global coordinate system; the minus sign follows from interface equilibrium.

For real k_x, the Bloch transformation matrix $\mathbf{T}(k_x)$ enforces the displacement condition in Eq. (39) through

$$\mathbf{u} = \mathbf{T}(k_x)\widetilde{\mathbf{u}} \tag{40}$$

For free-wave propagation, boundary-force equilibrium and zero applied loads at the internal nodes give $\mathbf{T}^{\mathrm{H}}\mathbf{f} = \mathbf{0}$. Substitution into Eq. (38) and premultiplication by $\mathbf{T}^{\mathrm{H}}$ therefore yield

$$\widetilde{\mathbf{K}}(k_x, \omega)\widetilde{\mathbf{u}} = \mathbf{0}, \qquad \widetilde{\mathbf{K}} = \mathbf{T}^{\mathrm{H}}\mathbf{K}(\omega)\mathbf{T} \tag{41}$$

where $\widetilde{\mathbf{u}}$ contains the independent unit-cell coordinates and H denotes the conjugate transpose. The eigenfrequencies are determined using the Wittrick–Williams algorithm (see section 3.3) at each prescribed wavenumber.

3.3. Wittrick-Williams algorithm

The dynamic stiffness matrices can now be utilized for eigenfrequency analysis for different cases including finite structures with classical and non-classical boundary conditions and periodic structures with Bloch periodic conditions. The eigenfrequency analysis requires that Eq. (41) be solved by evaluating the zeros of the determinant of $\widetilde{\mathbf{K}}(\omega)$. But the transcendental form of the eigenvalue problem is prone to numerical ill-conditioning and can miss closely spaced natural frequencies. However, this problem can be solved using an efficient and powerful technique called the Wittrick-Williams algorithm [60]. Using the Sturm sequence property, the algorithm computes the total number of natural frequencies $J(\omega^*)$ below a considered trial frequency ω^* as

$$\begin{aligned} J(\omega^*) &= J_0(\omega^*) + s\Big\{\widetilde{\mathbf{K}}(\omega^*)\Big\} \\ &= \sum_{k=1}^{n_f} J_k(\omega^*) + s\Big\{\widetilde{\mathbf{K}}(\omega^*)\Big\} \end{aligned} \tag{42}$$

where $s\{\widetilde{\mathbf{K}}(\omega^*)\}$ is the sign count of the DSM of the overall structure $\widetilde{\mathbf{K}}$, J_k is the number of natural frequencies between 0 and ω^* for k^{th} frame component with its ends fully clamped and n_f is the total number of frame components in the structure.

4. Dispersion characteristics of the unit cell

The band structure of the X-TCLR unit cell with $L_r = 21$ mm is computed using the spectral finite element method described in section 3. For the undamped reciprocal lattice, symmetry about $k_x = 0$ allows the dispersion

curves to be obtained by varying the Bloch wavenumber over the positive half of the one-dimensional first Brillouin zone, from $k_x = 0$ to the zone boundary at $k_x = \pi/a$. For presentation, the wave vector is normalised with respect to the Brillouin-zone boundary. The first six dispersion branches are presented in Fig. 4, where the shaded regions indicate two complete bandgaps. The first extends from 3420.21 Hz (P_3) to 3618.67 Hz (P_4). The second, considerably wider gap extends from 4589.67 Hz (P_5) to 6751.54 Hz (P_6). Moreover, a flat branch at 5460.29 Hz also appears inside the second bandgap region which coincides with the first natural frequency of a cantilever beam of same length L_r and cross-section. The group velocity of a Bloch branch is

$$v_g = \frac{\partial \omega}{\partial k_x} = 2\pi \frac{\partial f}{\partial k_x}. \tag{43}$$

A horizontal dispersion branch is associated with a small group velocity and weak spatial propagation of the corresponding Bloch mode. However, the associated mode shape must also be examined to identify whether the flat branch represents deformation localised within the resonators.

The flexural Bloch modes at P_1, P_2 and P_5–P_7, marked in Fig. 4, are examined to interpret the first branch and the locally resonant bandgap. The mode shapes are presented in Fig. 5, where the black and coloured geometries represent the undeformed and deformed unit cells, respectively. Colour indicates the normalised out-of-plane displacement, with the colorbar shown in Fig. 5(f).

Points P_1 and P_2 lie on the first branch at $k_x = 0$ and $k_x = \pi/a$, respectively. At P_1, the unit cell undergoes rigid-body motion without flexural strain (Fig. 5(a)). At P_2 (751.90 Hz), flexural deformation occurs mainly along the primary beam, while the cantilever resonators remain nearly un-

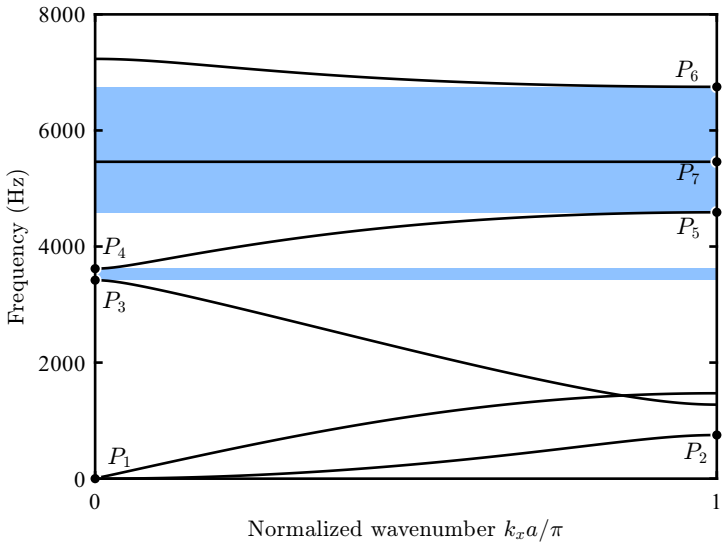


Figure 4: Band structure of the X-TCLR unit cell with $L_r = 21$ mm. The shaded regions indicate the first bandgap and the second locally resonant bandgap, which contains a flat resonator-dominated branch.

deformed (Fig. 5(b)). This indicates that the first branch is dominated by flexural motion of the primary beam.

The modes at P_5 (4589.67 Hz) and P_6 (6751.54 Hz) correspond to the lower and upper boundaries of the second bandgap, respectively (Fig. 5(c,d)). Both modes exhibit pronounced bending of the cantilever resonators, accompanied by different deformation patterns in the primary beam. At P_7 (5460.29 Hz), the deformation is strongly concentrated in the cantilever resonators, while the primary beam remains nearly stationary (Fig. 5(e)). This mode belongs to the flat dispersion branch, whose frequency closely matches the first bending natural frequency of the isolated cantilever. The spatial confinement of the deformation in the local resonators and the zero slope of the corresponding dispersion branch strongly support the interpretation that

the second bandgap is governed by local resonance.

5. Numerical analysis of frequency-selective localisation

5.1. Tuning the locally resonant bandgap

This study focuses on tuning the LRBG by varying the inclined cantilever arm L_r of the X-TCLR unit cell. L_r is varied from 21 to 24 mm, while all other properties listed in Table 1 remain unchanged. Fig. 6 shows the resulting changes in the upper edge of the fourth branch, the flat fifth branch, and the lower edge of the sixth branch. As L_r increases, the cantilevers become more flexible and their first bending natural frequency decreases. The flat fifth branch follows the same trend: at each L_r, its frequency matches the first bending natural frequency of an isolated cantilever with the corresponding length and cross-section. Accordingly, the locally resonant bandgap shifts to lower frequencies, from 4589.67 Hz–6751.54 Hz at $L_r = 21$ mm to approximately 3797.24 Hz–5482.60 Hz at $L_r = 24$ mm.

Fig. 7 shows how the fourth dispersion branch changes with L_r. The wave number is normalised by the Brillouin-zone boundary as

$$\kappa = \frac{k_x a}{\pi}, \qquad 0 \leq \kappa \leq 1. \tag{44}$$

In terms of κ, the group velocity is

$$v_g = 2\pi \frac{\partial f}{\partial k_x} = 2a \frac{\partial f}{\partial \kappa}. \tag{45}$$

The slope of dispersion branches therefore gives a scaled group velocity. As L_r increases, the fourth branch moves to lower frequencies throughout the Brillouin zone, with a more pronounced shift near $\kappa = 1$. This trend is consistent with the lower bending frequency of the longer cantilevers. Each of the

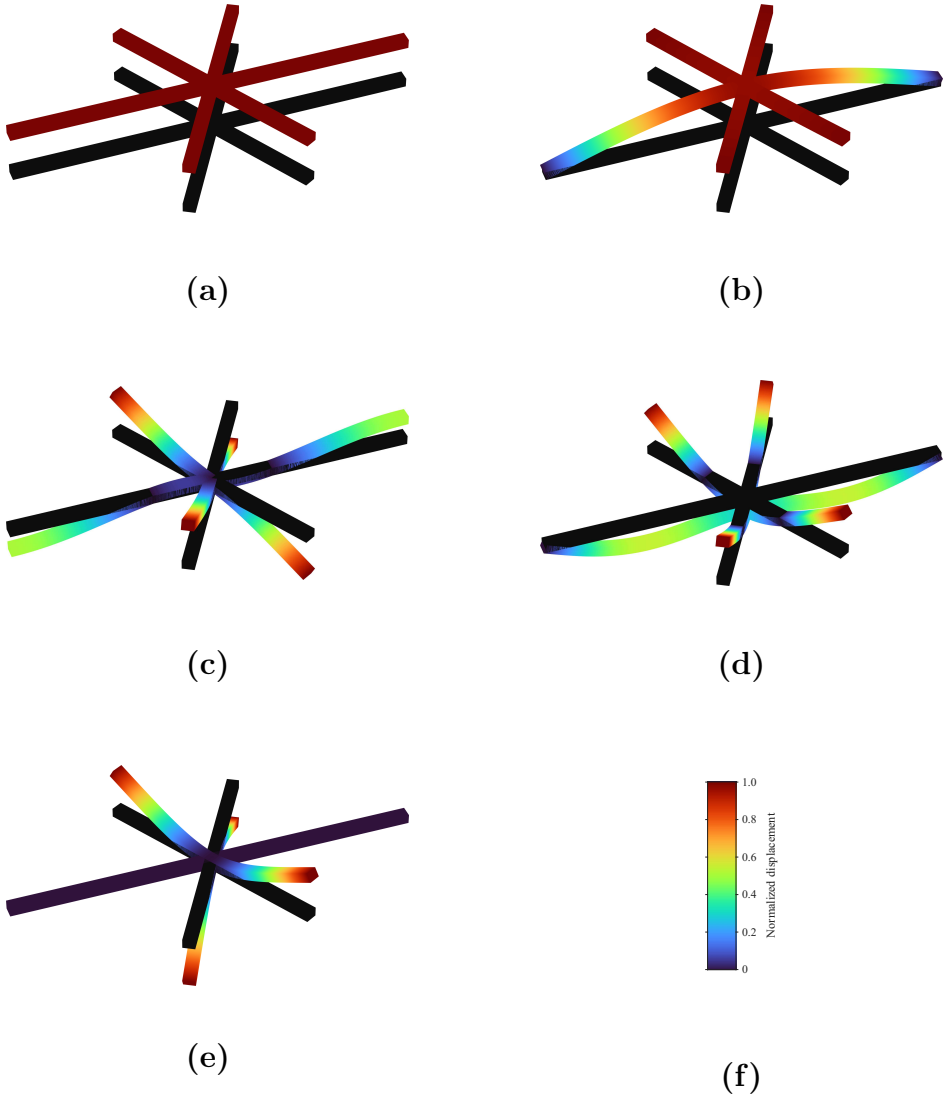


Figure 5: Bloch mode shapes of the X-TCLR unit cell at selected points in the dispersion diagram: (a) P_1 at the Brillouin zone centre and (b) P_2 at the Brillouin zone boundary, both corresponding to the first dispersion branch; (c) P_5 and (d) P_6, corresponding to the lower and upper edges of the locally resonant bandgap, respectively; (e) P_7, corresponding to the flat locally resonant branch; and (f) the common normalised out-of-plane displacement scale.

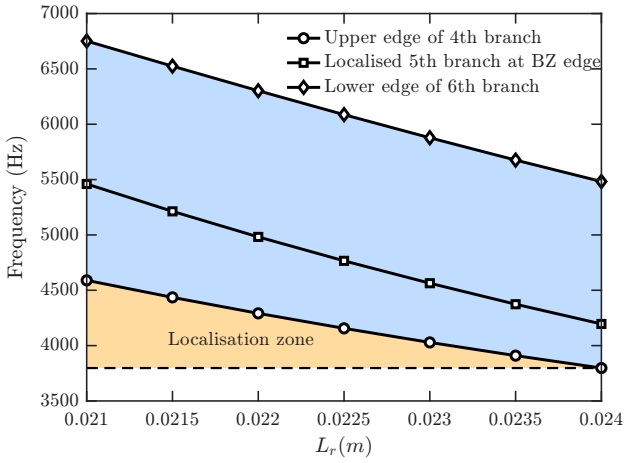


Figure 6: Variation of the LRBG with inclined resonator arm length L_r. The upper edge of the fourth branch forms the lower boundary of the gap, the flat fifth branch follows the first bending resonance of the cantilever, and the lower edge of the sixth branch forms the upper boundary.

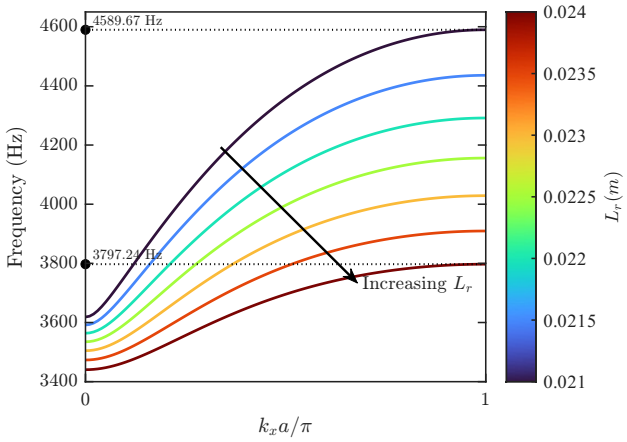


Figure 7: Evolution of the fourth dispersion branch as the inclined resonator-arm length L_r increases from 21 to 24 mm. The upper band-edge frequency decreases with increasing L_r, while the group velocity approaches zero near the Brillouin-zone boundary $\kappa = 1$.

fourth dispersion branch approaches a horizontal tangent at $\kappa = 1$, where its group velocity tends to zero. Increasing L_r thus changes the frequency of this zero-group-velocity band edge, from 4589.67 Hz at 21 mm to approximately 3797.24 Hz at 24 mm. The horizontal dotted lines project the zero-group-velocity band-edge frequencies at $\kappa = 1$ for $L_r = 21$ and 24 mm onto the frequency axis. The black markers identify these frequencies, 4589.67 Hz and 3797.24 Hz, respectively, which delimit the tuning range of the upper edge of the fourth branch.

5.2. Localisation in the rainbow meta-lattice

To investigate frequency-selective localisation of flexural waves, a rainbow meta-lattice is considered as shown in Fig. 8.

The finite meta-lattice comprises $N_c = 7$ unit cells, with the resonator-arm length L_r increasing from 21 mm at the left end to 24 mm at the right end in uniform increments of 0.5 mm, while all other geometric and material properties remain unchanged. Each unit cell is interpreted through its local dispersion relation: the dispersion that would be obtained by periodically repeating a unit cell with that cell's L_r. The dispersion curves for $L_r = 21, 21.5, \ldots, 24$ mm therefore represent the locally periodic counterparts of cells 1–7, respectively. Their fourth-branch upper edges coincide with the lower LRBG edges in Fig. 6 and decrease from 4589.67 Hz to 3797.24 Hz along the lattice, linking L_r grading to a spatial variation of the local propagation limit. The associated region for rainbow localisation (3797.24 Hz - 4589.67 Hz) is shaded orange in Fig. 6, bounded above by the fourth-branch upper-edge curve and below by its minimum edge frequency at $L_r = 24$ mm.

Consider a fixed excitation frequency f^* within this rainbow trapping

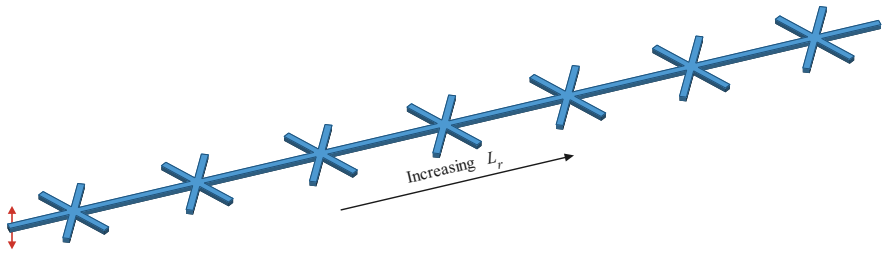


Figure 8: Schematic of the seven-unit-cell graded X-TCLR rainbow meta-lattice with L_r increasing from 21 to 24 mm along the direction of grading. The transverse harmonic excitation is applied at the left end.

zone. It lies below the local fourth-branch edge at the excited end and can therefore propagate into the lattice. As L_r increases from cell to cell, the local fourth-branch edge moves down towards f^*. On the local dispersion curve, the wave number corresponding to f^* consequently approaches $\kappa = 1$, where the curve becomes flat. Its local group velocity progressively decreases and reaches zero if f^* coincides with a cell's band-edge frequency. The wave thus slows and its response concentrates near that turning cell; farther along the lattice, f^* lies above the local fourth-branch edge (bandgap) and the response decays. Higher frequencies reach this condition closer to the excited end, whereas lower frequencies travel farther before slowing.

To assess the spatial response of the seven-cell graded meta-lattice, a harmonic transverse displacement was prescribed at the left-end node, normal to the plane of the lattice. The end rotations were free, and the opposite end was free. The complex displacement amplitudes were obtained by solving Eq. 38, subject to the prescribed transverse displacement at the left-end node. Fig. 9 shows the normalised transverse displacement fields and cell-wise localisation profiles at six selected excitation frequencies. At 3805 Hz,

the largest response occurs in cell 6. As the frequency increases through 3930, 4035, 4179, and 4345 Hz, the dominant response moves successively to cells 5, 4, 3, and 2; at 4545 Hz, it occurs in cell 1. The response thus shifts towards the excited end with increasing frequency, consistent with higher-frequency waves approaching their local fourth-branch edges earlier in the graded lattice. The selected frequencies and dominant cells are summarised in Table 2. The selected-frequency response profiles focus on unit cells 1–6, where the reduction in flexural response beyond the localised unit cell can be examined before the lattice terminates at the free end of unit cell 7.

Table 2: Frequency-selective spatial localisation in the rainbow meta-lattice: dominant unit cells and corresponding localisation factors at selected excitation frequencies.

Frequency (Hz)	3805	3930	4035	4179	4345	4545
Peak unit cell	6	5	4	3	2	1
Localisation factor	0.364	0.386	0.388	0.464	0.569	0.841

The localisation profiles quantify the mass-weighted transverse displacement within each cell. The response measure for cell j is

$$\mathcal{M}_j(f) = \sum_{e \in \mathcal{C}_j} \rho A L_e \frac{|w_{e1}(f)|^2 + |w_{e2}(f)|^2}{2}, \tag{46}$$

where L_e is the length of element e, w_{e1} and w_{e2} are its end-node transverse displacements, and $\mathcal{C}_j$ is the set of elements assigned to cell j. An element is assigned to the cell containing its midpoint and is therefore counted only once. The corresponding localisation fraction is

$$\eta_j(f) = \frac{\mathcal{M}_j(f)}{\sum_{q=1}^{N_c} \mathcal{M}_q(f)}, \qquad \sum_{j=1}^{N_c} \eta_j(f) = 1. \tag{47}$$

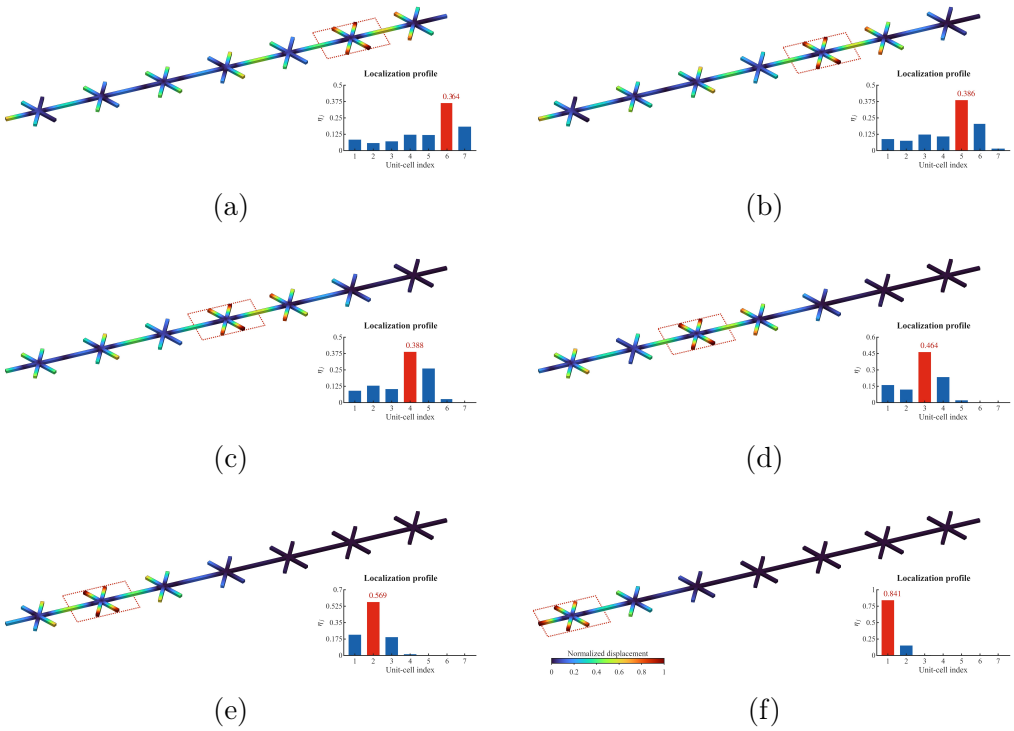


Figure 9: Numerically (SFEM) obtained spatial distributions of normalised transverse displacement response and corresponding unit-cell localisation factors at (a) 3805 Hz, (b) 3930 Hz, (c) 4035 Hz, (d) 4179 Hz, (e) 4345 Hz, and (f) 4545 Hz.

At a fixed frequency, η_j is also the cell's fraction of the transverse kinetic-energy measure under the nodal lumped-mass approximation, since the common frequency factor cancels upon normalisation. The dominant cell is $j^*(f) = \arg\max_j \eta_j(f)$, and its fraction is $\eta_{\max}(f) = \eta_{j^*}(f)$. In Fig. 9, the dashed red outline marks j^* on the displacement field, while the red inset bar and its numerical label show $\eta_{\max}$. For example, these fractions are 0.364 for cell 6 at 3805 Hz and 0.386 for cell 5 at 3930 Hz.

The six response fields in Fig. 9 illustrate localisation at selected frequencies. To assess the frequency-selective localisation behaviour across a wider

and continuous range, the cell-wise localisation fraction $\eta_j(f)$ is evaluated from 3650 Hz to 4550 Hz and plotted in Fig. 10. Each colour value gives the fraction of the total mass-weighted transverse response contained in a particular unit cell at that frequency. Across the rainbow-trapping range predicted by the local dispersion analysis, the localisation shifts systematically from cell 6 at lower frequencies towards cell 1 at higher frequencies. The ridge in the localisation map advances in steps because position is resolved by unit cell, while each cell remains the dominant response location over a finite frequency interval.

Table 3: Frequency intervals of dominant spatial localisation in individual unit cells of the rainbow meta-lattice, obtained from the numerical localisation map in Fig. 10.

Peak cell, j^*	1	2	3	4	5	6
Frequency interval (Hz)	4408.5–4550.0	4270.1–4405.5	4137.6–4267.1	4014.2–4134.6	3899.8–4011.2	3767.4–3896.8

As summarised in Table 3, unit cell 6 has the largest localisation fraction over approximately 3767–3897 Hz. With increasing excitation frequency, the dominant response shifts successively to cells 5, 4, 3, 2, and 1, with unit cell 1 dominant over approximately 4409–4550 Hz. This ordered frequency–position separation demonstrates frequency-selective localisation of flexural waves in the rainbow meta-lattice. Within the frequency range examined, the localisation intervals observed for unit cells 1–6 lie predominantly within the trapping range inferred from local dispersion. As L_r increases along the lattice, the upper edge of the local fourth branch decreases and approaches higher excitation frequencies nearer the excited end and lower excitation frequencies farther along the lattice. The weaker response beyond the dominant cell is consistent with attenuation in subsequent cells whose local bandgaps

contain the excitation frequency. The localisation intervals differ slightly from estimates based on infinitely repeated unit cells because coupling between cells of different L_r and the end conditions influence the harmonic response of the meta-lattice.

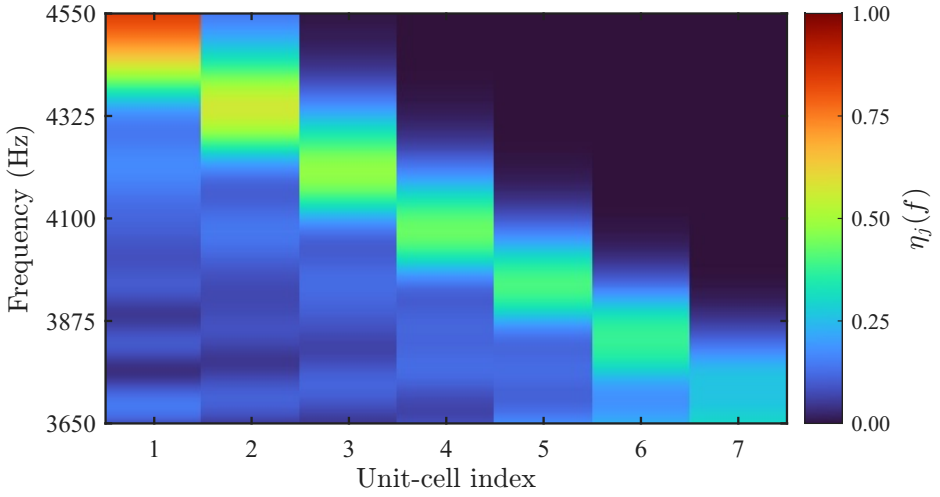


Figure 10: Numerically (SFEM) obtained frequency–unit-cell localisation map of the mass-weighted transverse displacement localisation fraction $\eta_j(f)$ in the seven-cell graded meta-lattice. The localisation ridge shifts from the left end ($L_r = 21$ mm) at higher frequencies towards the right end ($L_r = 24$ mm) at lower frequencies.

6. Experimental validation of frequency-selective localisation

To experimentally validate the numerically predicted frequency-selective localisation, the out-of-plane flexural response of a fabricated seven-cell graded meta-lattice made of mild steel, shown in Fig. 11b, was investigated using the experimental setup illustrated in Fig. 11a. An extended end portion of the specimen was fastened to the electromagnetic shaker using two bolts, while the opposite end remained free. The shaker provided transverse base

excitation normal to the plane of the meta-lattice. For the selected frequency tests, a sinusoidal signal at a fixed frequency f was generated and amplified to drive the shaker, imposing low-amplitude out-of-plane harmonic motion at the clamp. A laser Doppler vibrometer measured the steady-state velocity sequentially at multiple locations across the lattice. The measured velocity amplitudes were used to construct the spatial response distribution at each excitation frequency.

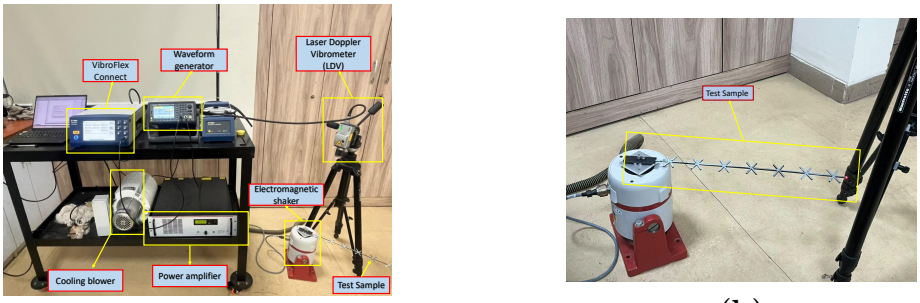


Figure 11: (a) Experimental setup and (b) meta-lattice specimen mounted on the electromagnetic shaker.

Fig. 12 presents the measured response distributions at the same six frequencies used in the SFEM analysis (see Table 2). At 3805 Hz, the largest response occurs in unit cell 6. As the frequency increases to 3930, 4035, 4179, and 4345 Hz, the dominant response moves successively to unit cells 5, 4, 3, and 2; at 4545 Hz, it is concentrated in cell 1. The localisation profiles accompanying the velocity fields identify these peak-response cells, while the reduced responses in subsequent cells are consistent with the local propagation limits predicted from the dispersion analysis. The experimentally observed sequence therefore reproduces the frequency-dependent spatial

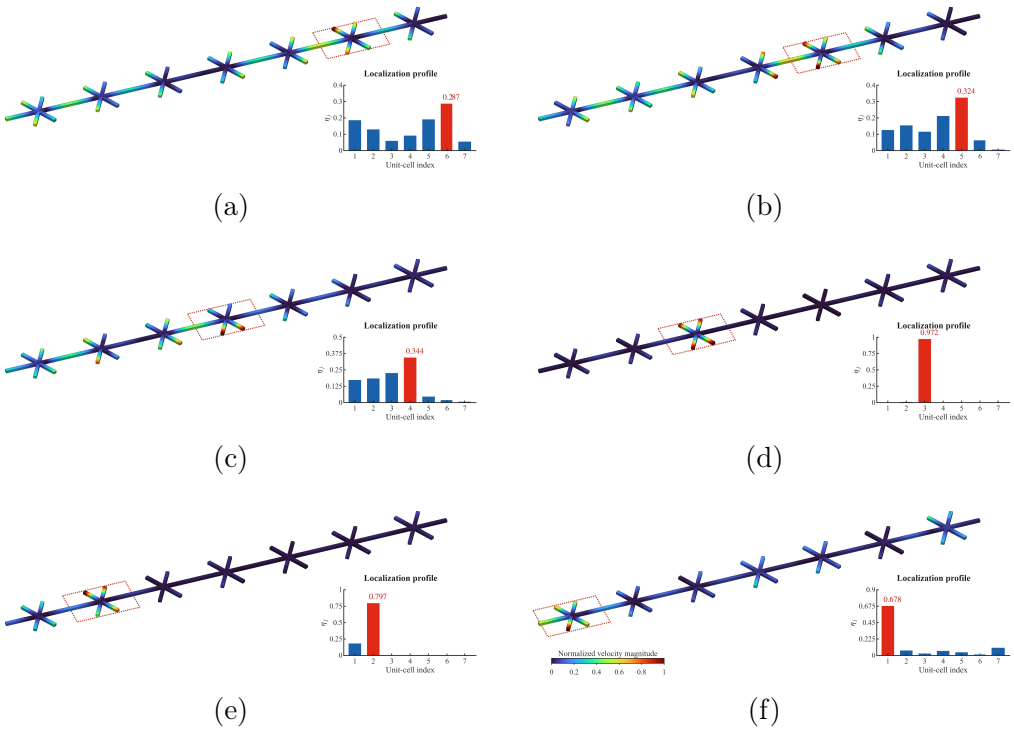


Figure 12: Experimentally measured spatial distributions of normalised transverse velocity response demonstrating frequency-selective localisation at (a) 3805 Hz, (b) 3930 Hz, (c) 4035 Hz, (d) 4179 Hz, (e) 4345 Hz, and (f) 4545 Hz.

ordering predicted by SFEM. For harmonic motion at a fixed frequency, velocity and displacement amplitudes differ by the spatially uniform factor $2\pi f$; their separately normalised fields can consequently be compared.

To examine the frequency intervals over which individual cells dominate, separate sinusoidal frequency-sweep measurements were performed over a range covering 3650–4550 Hz. The recorded velocity time histories were transformed into frequency-domain spectra using the fast Fourier transform (FFT). At each frequency, the velocity spectral magnitudes were used to evaluate the cell-wise localisation fractions with the same mass weighting

and normalisation employed in the numerical analysis. These fractions were assembled into the frequency–unit-cell localisation map shown in Fig. 13.

The experimental map reproduces the spatial progression predicted in Fig. 10: higher-frequency responses are concentrated in cells with smaller L_r near the excited end, whereas lower-frequency responses are localised in cells with larger L_r farther along the lattice. This progression is consistent with the L_r-dependent shift of the local fourth-band edge.

Table 4 compares the experimentally observed and SFEM-predicted frequency intervals of dominant localisation for cells 1–6. The measured response distributions and frequency–position localisation map reproduce the predicted ordering of the dominant unit cells, although differences occur in the boundaries of individual intervals. To quantify this agreement, the midpoint of each experimentally identified interval is compared with the midpoint of the corresponding SFEM interval. The mean absolute midpoint difference for the six cells is approximately 56.7 Hz, corresponding to a mean relative difference of 1.38% with respect to the SFEM midpoint frequencies. These values characterise the agreement of the localisation-interval positions rather than the complete spatial response distributions. The numerical–experimental comparison supports the interpretation that resonator-length grading produces an ordered frequency-dependent distribution of flexural vibration in the fabricated finite meta-lattice.

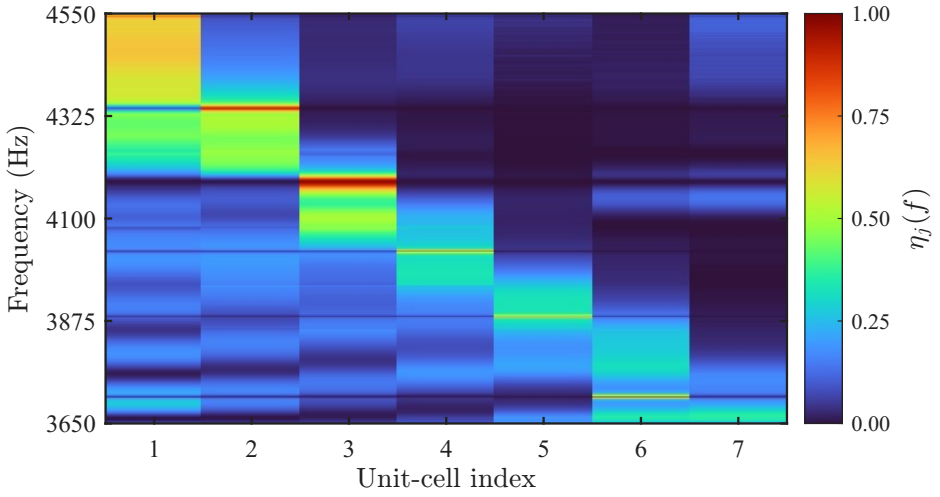


Figure 13: Experimentally obtained frequency–unit-cell localisation map of the mass-weighted transverse velocity localisation fraction $\eta_j(f)$ in the seven-cell graded meta-lattice. The localisation ridge shifts from the left end ($L_r = 21$ mm) at higher frequencies towards the right end ($L_r = 24$ mm) at lower frequencies.

Table 4: Comparison of experimentally observed and SFEM-predicted frequency intervals of dominant unit-cell localisation. Narrow transition intervals in which neighbouring cells exhibit comparable localisation fractions are omitted from the experimental ranges.

Cell, j^*	1	2	3	4	5	6
SFEM (Hz)	4408.5–4550.0	4270.1–4405.5	4137.6–4267.1	4014.2–4134.6	3899.8–4011.2	3767.4–3896.8
Experiment (Hz)	4354.3–4550.0	4203.8–4351.3	4047.3–4200.8	3957.0–4044.3	3863.7–3948.0	3707.2–3854.7

7. Conclusion

This study investigated frequency-selective localisation of out-of-plane flexural waves in a graded planar meta-lattice comprising X-TCLR unit cells. The integral configuration consists of inclined cantilever resonators connected to a continuous primary beam, enabling geometric tuning of local dynamic characteristics through the resonator-arm length. The spectral finite element

method (SFEM), incorporating Timoshenko flexure and Saint–Venant torsion, was employed to investigate the unit-cell dispersion and finite-lattice harmonic responses. Its frequency-dependent dynamic stiffness formulation enabled these analyses without requiring fine spatial discretisation of the constituent members. The Bloch dispersion of the reference unit cell with $L_r = 21$ mm identified a first bandgap extending from 3420.21 to 3618.67 Hz and a second bandgap (LRBG) spanning 4589.67–6751.54 Hz. The latter contained a nearly flat dispersion branch at 5460.29 Hz, whose frequency closely corresponded to the first bending natural frequency of the isolated cantilever, with deformation concentrated in the resonator arms.

Increasing the inclined cantilever-arm length L_r from 21 to 24 mm shifted the lower edge of the LRBG from 4589.67 to 3797.24 Hz. The corresponding upper edge of the fourth dispersion branch approached zero group velocity at the Brillouin-zone boundary. This geometrically controlled shift provided a dispersion-based estimate of the frequency range relevant to spatial localisation. Importantly, the tuning was achieved while preserving the primary-beam geometry, member cross-sections and unit-cell spacing.

Steady-state harmonic analysis of the seven-cell graded meta-lattice revealed an ordered frequency–position relationship, with the dominant flexural response shifting from cell 6 at 3805 Hz to cell 1 at 4545 Hz. The cell-wise localisation fractions and frequency–position maps quantified this progression and identified finite frequency intervals over which successive unit cells exhibited the largest responses. The results established a connection between the spatial variation of local propagation limits and the distribution of flexural vibration within the finite structure.

Experiments on the fabricated graded meta-lattice reproduced the numerically predicted ordering of dominant unit cells at the six selected excitation frequencies. The experimentally obtained localisation map further confirmed the progression of dominant response locations over the investigated frequency range. The measured localisation intervals occupied comparable frequency regions to the SFEM predictions, with a mean absolute difference of approximately 56.7 Hz between the corresponding interval midpoints. The remaining discrepancies may reflect differences in mounting conditions, fabrication tolerances and other experimental uncertainties.

The combined dispersion, finite-lattice and experimental results demonstrate that geometric grading of integral cantilever resonators provides a means of controlling the spatial distribution of flexural vibration over distinct frequency intervals. The resulting frequency–position relationship establishes a basis for designing resonant structural lattices with preferential vibration response at prescribed locations, with potential applications in frequency-selective sensing and vibration energy harvesting.

CRediT authorship contribution statement

Subhasish Sarkar: Conceptualization, Methodology, Software, Formal analysis, Investigation, Validation, Data curation, Visualization, Writing – original draft.

Avinash Umashankar: Investigation, Methodology, Data curation.

Srinivasan Gopalakrishnan: Methodology, Supervision, Writing – review & editing.

Acknowledgements

The authors gratefully acknowledge Dr. Rajesh Chaunsali, Assistant Professor in the Department of Aerospace Engineering at the Indian Institute of Science, for providing access to the Laboratory for Engineered Materials & Structures (LEMS) to conduct the experiments reported in this study.

Data availability

The data that support the findings of this study are available from the corresponding author upon reasonable request.

Competing interests

The authors declare that they have no competing interests.

References

[1] W. Elmadih, D. Chronopoulos, J. Zhu, Metamaterials for simultaneous acoustic and elastic bandgaps, Scientific reports 11 (1) (2021) 14635.

[2] G. L. Chen, Z. Tao, Y. M. Luo, Y. Zhang, Y. Pan, D. Han, F. Y. Ma, R. Zhu, X. Ren, Auxetic hybrid metamaterial with tunable elastic wave bandgap, Smart Materials and Structures 33 (7) (2024) 075013.

[3] A. Burlon, G. Failla, Wave propagation and bragg gaps formation in periodically supported coupled bending-torsional thin-walled beams, Thin-Walled Structures 216 (2025) 113496.

[4] D. E. Quadrelli, J. Marconi, F. Braghin, A. Erturk, Subwavelength negative refraction and flexural wave lens design via resonant double-negative piezoelectric metamaterial, Smart Materials and Structures 33 (2) (2024) 025005.

[5] Y. Hu, M. Li, H. Liu, B. Li, Broadband manipulation of flexural waves based on phase-modulated elastic metasurfaces, Engineering Structures 275 (2023) 115209.

[6] G. Wang, Y. Guan, Z. Chen, Z. Zhou, X. Xu, C. Lim, W. Chen, Frequency-dependent elastic wave filtration and separation by hexagonal topological phononic crystals, Composite Structures (2025) 119289.

[7] X. An, X. Yuan, H. Fan, Meta-kagome lattice structures for broadband vibration isolation, Engineering Structures 277 (2023) 115403.

[8] Z. Wang, Z. Liu, S. Zhang, L. Gao, X. Liang, B. Liang, Y. Wen, Multi-functional hollow lattice metamaterials with broadband vibration isolation and high stiffness and strength, Engineering Structures 341 (2025) 120873.

[9] E. Panahi, A. Hosseinkhani, M. F. Khansanami, D. Younesian, M. Ranjbar, Novel cross shape phononic crystals with broadband vibration wave attenuation characteristic: Design, modeling and testing, Thin-Walled Structures 163 (2021) 107665.

[10] G. Yan, S. Yao, Y. Li, Propagation of elastic waves in metamaterial plates with various lattices for low-frequency vibration attenuation, Journal of Sound and Vibration 536 (2022) 117140.

[11] Q. Geng, M. Wang, X. Zhou, X. Yang, Z. Shao, Y. Li, In-plane auxeticity and flexural wave attenuation characteristics of metamaterial plates with peanut-crescent-shaped perforations, Thin-Walled Structures (2025) 114443.

[12] Y. Li, E. Baker, T. Reissman, C. Sun, W. K. Liu, Design of mechanical metamaterials for simultaneous vibration isolation and energy harvesting, Applied Physics Letters 111 (25) (2017).

[13] J. Wang, X. Yang, X. Zhang, Z. Chen, C. Lim, Enhancement of flexural wave energy harvest in lightweight subwavelength defective metamaterial lattices, Journal of Sound and Vibration (2026) 119841.

[14] W. Lu, R. Dai, S. Chang, C. Li, Z. Chen, Low-frequency metamaterial with enhanced vibration energy harvesting and its multi-objective optimization, Journal of Vibration Engineering & Technologies 14 (7) (2026) 479.

[15] Y. Zhou, L. Ye, W. Chen, Impact mitigation performance of hybrid metamaterial with a low frequency bandgap, International Journal of Mechanical Sciences 213 (2022) 106863.

[16] S. Datta, X. Shi, S. Mukherjee, Y. Deng, L. Udpa, Model-based study of a metamaterial lens for nondestructive evaluation of composites, Journal of Nondestructive Evaluation, Diagnostics and Prognostics of Engineering Systems 3 (4) (2020) 041001.

[17] C. Wang, X. Yao, G. Wu, L. Tang, Complete vibration band gap charac-

teristics of two-dimensional periodic grid structures, Composite Structures 274 (2021) 114368.

[18] Y. Iwata, T. Yokozeki, Shock wave filtering of two-dimensional cfrp x-lattice structures: A numerical investigation, Composite Structures 265 (2021) 113743.

[19] K. Zhang, P. Zhao, C. Zhao, F. Hong, Z. Deng, Study on the mechanism of band gap and directional wave propagation of the auxetic chiral lattices, Composite Structures 238 (2020) 111952.

[20] H.-y. Yang, S.-l. Cheng, X.-f. Li, Q. Yan, B. Wang, Y.-j. Xin, Y.-t. Sun, Q. Ding, H. Yan, Y.-j. Li, et al., Study on the bandgap and directional wave propagation mechanism of novel auxiliary semicircle rings lattices, Materials Today Communications 35 (2023) 105680.

[21] Z. Zhang, A. Wang, Q. Lin, Y. Sun, B. Wang, L. Wang, S. Wang, Y. Wu, Y. Ma, Q. Ding, Study on the multi-low-frequency band gaps and vibration reduction performance of the tooth-shaped acoustic metamaterial, European Journal of Mechanics-A/Solids 109 (2025) 105462.

[22] Q. Cheng, H. Guo, T. Yuan, P. Sun, F. Guo, Y. Wang, Topological design of square lattice structure for broad and multiple band gaps in low-frequency range, Extreme Mechanics Letters 35 (2020) 100632.

[23] H. Lin, J. Wang, H. Feng, X. Chang, D. Cao, Mechanical properties and band gap generation mechanism of a novel negative poisson's ratio chiral metamaterial structure, International Journal of Structural Stability and Dynamics (2025) 2750152.

[24] S. Wen, Y. Xiong, S. Hao, F. Li, C. Zhang, Enhanced band-gap properties of an acoustic metamaterial beam with periodically variable cross-sections, International Journal of Mechanical Sciences 166 (2020) 105229.

[25] S. R. Patro, A. Banerjee, G. Ramana, Vibration attenuation characteristics of finite locally resonant meta beam: Theory and experiments, Engineering Structures 278 (2023) 115506.

[26] Y. Xiao, J. Wen, Closed-form formulas for bandgap estimation and design of metastructures undergoing longitudinal or torsional vibration, Journal of Sound and Vibration 485 (2020) 115578.

[27] G. Mahajan, A. Mukherjee, A. Banerjee, Influence of attached inertia and resonator on the free wave propagation in 2d square frame grid lattice metamaterial, Waves in Random and Complex Media 34 (5) (2024) 4381–4408.

[28] H. Jafari, S. Sepehri, M. R. H. Yazdi, M. M. Mashhadi, M. M. S. Fakhrabadi, Hybrid lattice metamaterials with auxiliary resonators made of functionally graded materials, Acta Mechanica 231 (2020) 4835–4849.

[29] X. An, H. Fan, C. Zhang, Elastic wave and vibration bandgaps in planar square metamaterial-based lattice structures, Journal of sound and vibration 475 (2020) 115292.

[30] S. El-Borgi, R. Fernandes, P. Rajendran, R. Yazbeck, J. Boyd, D. Lagoudas, Multiple bandgap formation in a locally resonant linear

metamaterial beam: Theory and experiments, Journal of Sound and Vibration 488 (2020) 115647.

[31] A. Burlon, G. Failla, Flexural wave propagation in locally-resonant beams with uncoupled/coupled bending-torsion beam-like resonators, International Journal of Mechanical Sciences 215 (2022) 106925.

[32] V. F. Dal Poggetto, F. Bosia, M. Miniaci, N. M. Pugno, Optimization of spider web-inspired phononic crystals to achieve tailored dispersion for diverse objectives, Materials & Design 209 (2021) 109980.

[33] P. Zhao, K. Zhang, F. Hong, Z. Deng, A resonator inspired by spider web for wave propagation in planar periodic lattice, Thin-Walled Structures 174 (2022) 109118.

[34] S. Zhang, J. Lou, H. Fan, J. Du, A nonlinear acoustic metamaterial beam with tunable flexural wave band gaps, Engineering Structures 276 (2023) 115379.

[35] X. Fan, X. Mao, Y. Dong, M. Shao, L. Wang, J. Wu, Low-frequency broadband bandgap of a tunable metamaterial beam with electromagnetic resonators: Numerical and experimental study, International Journal of Structural Stability and Dynamics (2026) 2750119.

[36] C. Xu, W. Chen, H. Zuo, R. Cheng, H. Hao, Metastructure-based system for microvibration mitigation, International Journal of Structural Stability and Dynamics 26 (20) (2026) 2750390.

[37] S. E. Soliman, M. Barlou, K. L. Tsakmakidis, Z. J. Wong, Rainbow

trapping for advanced wave control, Advances in Physics: X 10 (1) (2025) 2517551.

[38] Z. Tian, L. Yu, Rainbow trapping of ultrasonic guided waves in chirped phononic crystal plates, Scientific reports 7 (1) (2017) 40004.

[39] A. Arreola-Lucas, G. Baez, F. Cervera, A. Climente, R. Méndez-Sánchez, J. Sánchez-Dehesa, Experimental evidence of rainbow trapping and bloch oscillations of torsional waves in chirped metallic beams, Scientific Reports 9 (1) (2019) 1860.

[40] C. Ellouzi, A. Zabihi, L. Gormley, F. Aghdasi, K. Stojanoska, A. Miri, R. Jha, C. Shen, Experimental demonstration of rainbow trapping of elastic waves in two-dimensional axisymmetric phononic crystal plates, The Journal of the Acoustical Society of America 155 (3) (2024) 1759–1766.

[41] B. Telgen, V. Kannan, J.-C. Bail, C. Dorn, H. Niese, D. M. Kochmann, Rainbow trapping of out-of-plane mechanical waves in spatially variant beam lattices, Journal of the Mechanics and Physics of Solids 191 (2024) 105762.

[42] H. Meng, D. Chronopoulos, N. Bailey, L. Wang, Investigation of 2d rainbow metamaterials for broadband vibration attenuation, Materials 13 (22) (2020) 5225.

[43] X. Feng, Z. Zhou, J. Xu, K. Li, P. Wang, J. Lai, Wave-structure conversion and rainbow trapping effect in complex cross-sectional structures, Mechanical Systems and Signal Processing 236 (2025) 113034.

[44] Y. Bao, L. Cai, C. Zheng, S. Ye, X. Xia, L. Hou, Z. Yao, X. Hu, X. Liu, Flexural wave trapping and vibration suppression of annular abh metasurfaces with radial periodicity, Mechanical Systems and Signal Processing 259 (2026) 114800.

[45] B. Wang, Y. Huang, W. Zhou, Z. Yang, Metamaterial beam for flexural wave resonance rainbow trapping and piezoelectric energy harvesting, Journal of Applied Physics 129 (6) (2021).

[46] T. Deng, L. Zhao, F. Jin, Flexural wave rainbow trapping effect in the periodic non-uniform euler-bernoulli beams and its application in energy harvesting, Mechanics of Materials 190 (2024) 104892.

[47] T. Deng, Q. Yan, F. Jin, N. Dong, H. Yan, L. Zhao, Rainbow trapping of flexural waves in nonuniform metamaterial beam induced by band gaps and interface states, Shock and Vibration 2026 (1) (2026) 4239842.

[48] W. Yuan, Y. Zhang, Y. Pan, Y. Huang, J. Zhao, F. Yang, Z. Zhong, Topological rainbow trapping, concentration and guiding in graded elastic valley phononic crystal plate, Engineering structures 304 (2024) 117596.

[49] X.-L. Tang, X.-Q. Zhang, T.-X. Ma, M. Kim, Y.-S. Wang, Topological rainbow trapping and broadband piezoelectric energy harvesting of acoustic waves in gradient phononic crystals with coupled interfaces, Applied Acoustics 233 (2025) 110630.

[50] R. Zheng, W. Xie, X. Wen, W. Deng, M. Ke, J. Lu, X. Huang, Z. Liu,

Capturing rainbow in on-chip phononic crystals, Physical Review Letters 137 (6) (2026) 066602.

[51] K. Chen, X. Dong, Z. Peng, G. Meng, Reconfigurable topological gradient metamaterials and potential applications, Thin-Walled Structures 205 (2024) 112572.

[52] D.-G. Zhao, Y. Li, X.-F. Zhu, Broadband lamb wave trapping in cellular metamaterial plates with multiple local resonances, Scientific reports 5 (1) (2015) 9376.

[53] J. M. De Ponti, L. Iorio, E. Riva, R. Ardito, F. Braghin, A. Corigliano, Selective mode conversion and rainbow trapping via graded elastic waveguides, Physical Review Applied 16 (3) (2021) 034028.

[54] J. M. De Ponti, L. Iorio, E. Riva, F. Braghin, A. Corigliano, R. Ardito, Enhanced energy harvesting of flexural waves in elastic beams by bending mode of graded resonators, Frontiers in Materials 8 (2021) 745141.

[55] J. Santini, C. Sugino, E. Riva, A. Erturk, Harnessing rainbow trapping via hybrid electromechanical metastructures for enhanced energy harvesting and vibration attenuation, Journal of Applied Physics 132 (6) (2022).

[56] W. Liu, J.-W. Chen, X.-Y. Su, Local resonance phononic band gaps in modified two-dimensional lattice materials, Acta Mechanica Sinica 28 (3) (2012) 659–669.

[57] O. Serrano, R. Zaera, J. Fernández-Sáez, On the mechanism of bandgap

formation in beams with periodic arrangement of beam-like resonators, Journal of Vibration and Acoustics 141 (6) (2019) 064503.

[58] S. Mukherjee, F. Scarpa, S. Gopalakrishnan, Phononic band gap design in honeycomb lattice with combinations of auxetic and conventional core, Smart Materials and Structures 25 (5) (2016) 054011.

[59] X. Liu, Z. Lu, S. Adhikari, Y. Li, J. R. Banerjee, Exact wave propagation analysis of lattice structures based on the dynamic stiffness method and the wittrick–williams algorithm, Mechanical Systems and Signal Processing 174 (2022) 109044. doi:10.1016/j.ymssp.2022.109044.

[60] W. H. Wittrick, F. W. Williams, A general algorithm for computing natural frequencies of elastic structures, The Quarterly Journal of Mechanics and Applied Mathematics 24 (3) (1971) 263–284. doi:10.1093/qjmam/24.3.263.